Macromolecules

Closing the Stability−Performance Gap in Organic Thermoelectrics by Adjusting the Partial to Integer Charge Transfer Ratio

Osnat Zapata-Arteaga,[†] Bernhard Dörling,[†] Aleksandr Perevedentsev,[†] Jaime Martín,[‡,§] J. Sebastian Reparaz,[†] and Mariano Campoy-Quiles*[,†]

[†]Institute of Materials Science of Barcelona (ICMAB-CSIC), Campus of the UAB, 08193 Bellaterra, Spain

[‡]POLYMAT and Polymer Science and Technology Department, Faculty of Chemistry, University of the Basque Country UPV/EHU, Manuel de Lardizabal 3, 20018 Donostia-San Sebastián, Spain

[§]Ikerbasque, Basque Foundation for Science, E-48011 Bilbao, Spain

Ⓢ Supporting Information

ABSTRACT: Two doping mechanisms are known for the well-studied materials poly(3-hexylthiophene) (P3HT) and poly(2,5-bis(3-alkylthiophen-2-yl)thieno[3,2-b]thiophene) (PBTTT), namely, integer charge transfer (ICT) and charge transfer complex (CTC) formation. Yet, there is poor understanding of the effect of doping mechanism on thermal stability and the thermoelectric properties. In this work, we present a method to finely adjust the ICT to CTC ratio. Using it, we characterize electrical and thermal conductivities as well as the Seebeck coefficient and the long-term stability under thermal stress of P3HT and PBTTT of different ICT/CTC ratios. We establish that doping through the CTC results in more stable, yet lower conductivity samples compared to ICT doped films. Importantly, moderate CTC fractions of ~33% are found to improve the long-term stability without a significant sacrifice in electrical conductivity. Through visible and IR spectroscopies, polarized optical microscopy, and grazing-incidence wide-angle X-ray scattering, we find that the CTC dopant molecule access sites within the polymer network are less prone to dedoping upon thermal exposure.
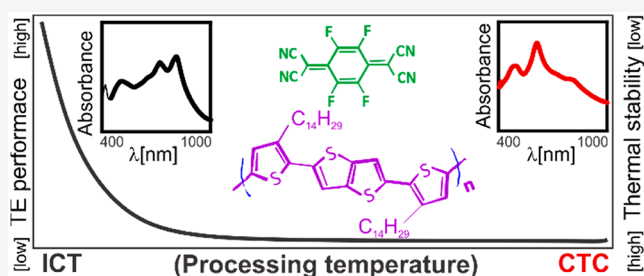
1. INTRODUCTION

Fine control of the doping level in organic semiconductors is necessary to optimize their electrical properties for applications such as thermoelectrics, transistors, and light-emitting devices. The realization of organic thermoelectric devices relies, indeed, on doping pristine organic semiconductors materials to tune their electrical conductivity (σ), Seebeck coefficient (α), and thermal conductivity (κ). Previous reports have explored the trade-off between these parameters to improve the dimensionless figure of merit $ZT = \alpha^2\sigma T/\kappa$,[1,2] where T stands for the absolute temperature.

Organic semiconductors were first doped by using alkali metals and halides, although their tendency to diffuse or react with the ambient or other layers has limited further development.[3] Molecular dopants have emerged as more promising candidates as they appear to be sufficiently stable for (at least short) lab tests. Particularly, dopant/host systems such as 2,3,5,6-tetrafluoro-7,7,8,8-tetracyanoquinodimethane (F4TCNQ) doped poly(2,5-bis(3-alkylthiophen-2-yl)-thieno-[3,2-b]thiophene) (PBTTT) have become materials test beds for studying the mechanisms involved in doping. Currently, two main doping mechanisms have been proposed, namely, integer charge transfer (ICT)[4] and charge transfer complex (CTC) formation.[5]

For p-type doping, charge transfer (δ) of effective charges is said to take place when the electron affinity of the dopant is higher than the ionization potential of the host ($EA_D > IP_H$).[6,7] Then a two-step process occurs, that is, (i) the transfer of one electron ($\delta = 1e$) from the host to the dopant, generating a ground state integer charge transfer (ICT), followed by (ii) thermal dissociation into a localized charge on the dopant and a mobile polaron on the host.[8] The alternative mechanism involves partial hybridization of the frontier orbitals between the dopant and host, creating new bonding and antibonding orbitals leading to a noninteger δ, often termed charge transfer complex (CTC).[9,10] Overall, the difference between both mechanisms suggests that CTCs need to interact with the unreacted host and then dissociate into free carriers; thus, an extra step is required compared to the ICT species.[10,11]

Evidence of these processes can be obtained by techniques such as optical absorption spectroscopy. For p-type doping, the ICT mechanism is characterized by the appearance of new subgap transitions from the localized radical anion (A$^-$ → A^{-*}) and two transitions from the mobile polaron (P$^+$ → P^{+*}) which, at high doping level, become a single transition from a

newly formed bipolaron $(BP^+ \rightarrow BP^{+*})$.[12] In the case of the CTC mechanism, the band gap between the newly formed orbitals is understood to follow a Hückel model:

$$E_{gap}^{CTC} = \frac{IP_H + EA_D}{2} \pm \sqrt{(IP_H - EA_D)^2 + 4\beta^2} \qquad (1)$$

which is affected by the IP_H, the EA_D, and a resonance integral β that changes exponentially with intermolecular distance and orientation.[13−18] For inferring the value of δ for tetracyanoquinodimethane (TCNQ) derivatives, IR spectroscopy is used as there is a shift to lower energies of the main $-C\equiv N$ stretch vibrational band upon charge transfer.[19,20] Moreover, rational synthetic design can provide highly specific physicochemical and electronic characteristics to certain molecular dopants and hosts,[18,21−24] whereby modifying their functional groups or size can effectively change their electron affinity, ionization potential, miscibility, and stability.[22,25,26]

Doping of P3HT and PBTTT with F4TCNQ is known to proceed predominantly by an ICT mechanism, yet exceptions have been reported for specific processing techniques[17] or suggested for very high dopant loadings.[19] For instance, early experiments on the F4TCNQ/quaterthiophene system awoke interest because it was found to follow a CTC mechanism ($\delta < 1$), even though ICT was expected due to the structural similarity to P3HT.[13] Subsequently, Jacobs et al. showed that increased temperature during codeposition of the F4TCNQ/P3HT system can, in fact, yield CTC, which was later attributed to a polymorph of P3HT.[17] In line with conventional theory, the electrical conductivity of such systems was lower than in the ICT case, which additionally showed very short lifetimes under ambient conditions. Moreover, recent experiments by Kiefer et al. demonstrated a particular case of "double doping" ($\delta = 2$) for some PBTTT derivatives doped with F4TCNQ. In their work, it was shown that a polymer with a sufficiently low IP is capable of donating a second electron to the new EA level of the F4TNQ radical anion.[6] On the other hand, Goetz et al. indicated that there is an optimal value between the degree of charge transfer δ and the peak electrical conductivity of small molecular semiconductors.[27] Whether conjugated polymers follow the same behavior remains an open question.

Long-term stability of doped conjugated polymers is highly desirable—a fact that has motivated numerous studies related to the diffusion and migration of the dopant within the polymer network and/or layers. Typically the dopant/host interactions are mostly weak van der Waals and Coulombic forces, which lead to the eventual dedoping of the polymer network.[28,29] It has also been suggested that the flexibility of the polymer backbone and the available space within the side chains dictate not only the doping limit but also the mobility and diffusion of the dopant.[30] To this end, several straightforward approaches to improve doping stability have been tested, such as the use of bulkier dopants[26] and modification of the chemical structure of dopants and/or hosts.[21,23,31] However, using bulkier dopant often carries processability penalties, while changing the chemical structure can lead to undesirable shifts of the respective energy levels.

Because the presence of ICT and/or CTC depends on a combination of energy levels and morphology, the doping method itself can also play a key role in determining their relative contributions. Currently, the "sequential processing method" is the most widely used one for molecular doping: it avoids processability issues inherent to the alternative "codeposition method" (e.g., complexation in solution[32] and thus a limit on the amount of dopant that can be added while maintaining solubility) and keeps morphology changes to a minimum.[32−34] This results in a comparatively high electrical conductivity due to the undisturbed morphology and concomitant good charge carrier mobility (μ) of oriented or semicrystalline polymers.[35,36] Typically the sequential methods involve doping a precast polymer film either from the vapor phase or from solutions in orthogonal solvents.[26,37,38] Contrary to codeposition, however, sequential methods do not offer precise control of the dopant loading and suffer from dopant diffusion limitations. This has motivated further developments of the related processing schemes that utilize photochemical, thermal, and reactive dedoping[33,39,40] to control the doping level and elsewhere optimization of multilayer processing techniques[41] to address the diffusion-limited problem. Specific processing methods that provide controlled ICT/CTC ratios are yet to be reported.

Here we demonstrate that controlling the substrate temperature and time during vapor doping results in a varying degree of the associated CTC and ICT states in the F4TCNQ/PBTTT system. (Where appropriate, comparisons are drawn with the more widely studied P3HT/F4TCNQ "reference" system to establish the generality of the findings.) Hence, this allows us to produce a set of samples with controlled ICT/CTC ratios and explore their thermoelectric performance and its stability under thermal stress. We find that samples processed to feature a moderate fraction of the CTC exhibit improved long-term stability without sacrificing electrical conductivity compared to samples where ICT dominates. These findings are rationalized by using extensive spectroscopic analysis as well as microscopy and structural characterization techniques. Importantly, since ICT and CTC doping mechanisms have been found in many different organic systems (see Table S1), our here presented conclusions regarding stability are likely to be very general.

2. MATERIALS AND METHODS

2.1. Materials and Sample Preparation. Poly(3-hexylthiophene) (P3HT; regioregular; $M_n = 50−100$ kDa) from Sigma-Aldrich, poly(2,5-bis(3-tetradecylthiophen-2-yl)-thieno[3,2-b]thiophene) (PBTTT-C14; hereafter termed PBTTT, $M_n = 50$ kDa) from 1-Material, and 2,3,5,6-tetrafluoro-7,7,8,8-tetracyanoquinodimethane (F4TCNQ) were purchased from TCI Chemicals. Chlorobenzene (>99%) was purchased from Sigma-Aldrich and conductive silver paint from RS Components. All chemicals were used as received.

Polymer films were fabricated from 30 mg/mL (P3HT) or 20 mg/mL (PBTTT) solutions in chlorobenzene. Solutions were stirred at 85 and 110 °C, respectively, for 3 h and used at this temperature for deposition. Films were deposited in ambient atmosphere by using a blade coater preheated at 110 °C, with a blade height of 200 μm at a speed of 30 mm/s. Finally, P3HT and PBTTT films were annealed at 150 and 180 °C, respectively, for 30 min and then allowed to cool slowly to room temperature. For vapor doping, a closed container beaker with similar dimensions to the setups reported in the literature[42,43] was chosen as a doping vessel (Figure S1) and a hot plate at 210 °C as the heat source. Then, large (~75 × 25 mm²) substrates precoated with polymer films were placed on the lid and exposed to F4TCNQ vapor for a doping time (t_d) of 5 and 50 min in ambient conditions. These samples are referred to in the upcoming text as partially and maximally doped, respectively (Figure S2). Dedoping of the maximally doped samples was done on a Kofler bench by using a continuous dedoping temperature (T_{dd}) range of 70−120 °C for a dedoping time (t_{dd}) of 20 min (Figure S1). Then they were sliced into several rectangular sections, as shown in Figure

S1. Each ~6 mm wide section is presumed to be quasi-homogeneous regarding the dopant content. Small deviations are expected either from thickness variations or from the Kofler bench, which exhibits a temperature gradient of 6.7 K/cm. Yet, this only results in a variation in temperature of ±2 K for each 6 mm wide sample. Samples doped while controlling the polymer substrate temperature were fabricated in a second setup, which, as seen in Figure S3, consisted of a modified reactor beaker with inbuilt heating elements.

2.2. Characterization. Vis−NIR spectra were measured by using both a Bruker HYPERION FTIR microscope connected to a VERTEX 70 spectrometer and a GES5E ellipsometer from Sopra/Semilab. The dopant content was estimated by integrating the main transitions of the F4TCNQ anion (A⁻), the neutral polymer (NP), Beer's law, and a known attenuation coefficient.[11,43] The fraction (χ) of CTC (χ_{CTC}) and ICT (χ_{ICT}) states was estimated as the ratio between the integrated intensity of their respective bands. IR spectroscopy was measured using a PerkinElmer Spectrum One spectrometer from 4000 to 500 cm^{-1}. The degree of charge transfer was calculated from the shift $\Delta\nu$ of the −C≡N stretch vibrational band, which is observed for tetracyanoquinodimethanes (TCNQ) derivatives upon electron transfer

$$\delta = \frac{2\Delta\nu}{\nu_0}\left[1 - \frac{\nu_1^2}{\nu_0^2}\right]^{-1} \tag{2}$$

where ν_0 and ν_1 correspond to the neutral and anion stretch modes, respectively.[19,44]

Raman spectra were taken with a WITec alpha 300 RA+ confocal microscope, coupled to an Olympus objective with 100× magnification (NA = 0.9), and excited with a 488 or 785 nm solid state laser.

The Seebeck coefficient and electrical conductivity were measured by using a custom-built setup with a four-probe configuration. All samples were sliced so that the typical sample area was approximately 20 mm × 6 mm. These were contacted with silver paint at the corners, which served as electrodes. Electrical conductivity was measured by using the van der Pauw method. Subsequently, for the Seebeck coefficient measurement, the temperature gradient between two contacts was slowly ramped from 0 to 40 K and measured with two T-type thermocouples, while the voltage was recorded with a Keithley 2400 SourceMeter. The Seebeck coefficient was extracted from a linear fit of the measured slope. The thickness of the deposited samples was determined by using a P16+ profilometer from KLA Tencor.

The thermal conductivity of the samples was measured by using a custom-built frequency-domain thermoreflectance setup which will be fully described in a future publication. In brief, a gold transducer with 60 nm thickness was thermally evaporated onto the surface of the samples. The wavelength of the pump and probe lasers was set at 405 and 532 nm, respectively, and the frequency range spanned between 1 kHz and 10 MHz. The maximum estimated temperature rise at the surface of the transducer was about 2 K. In simple words, a sinusoidal high-power excitation at 405 nm (about 2 mW) was focused onto the surface of the transducer, creating a local sinusoidal temperature oscillation. The resulting sinusoidal surface temperature wave was monitored through the low-power probe laser. Finally, the phase lag between the pump harmonic waves was measured by using a lock-in amplifier and modeled by numerically solving the spherical heat equation. Thus, fitting of the phase lag vs the applied frequency renders the thermal conductivity of the thin films. A general detailed description of the operational principle of this approach can be found elsewhere.[45]

Grazing incidence wide-angle X-ray scattering (GIWAXS) experiments were conducted at the NCD-SWEET beamline in ALBA synchrotron (Spain). The thin films were typically exposed for 1−5 s to an X-ray beam with a wavelength of 0.998 Å at an incidence angle 0.12°. 2D scattering patterns were collected by employing a WAXS LX255-HS detector from Rayonix (pixel size = 40 μm),

3. RESULTS AND DISCUSSION

3.1. Doping Method To Obtain a Desired CTC/ICT Ratio. Owing to the success of doping from the vapor phase and thermally induced dedoping, we employ these methods together with the use of temperature gradients for the dedoping of F4TCNQ/P3HT and F4TCNQ/PBTTT systems. As a first series of experiments, we prepared samples following the protocols established in the literature and thereafter investigated which processing parameters are relevant for the formation of CTC and/or ICT states. For this, our "maximally doped" samples (see the Materials and Methods section for details) of P3HT and PBTTT were dedoped by thermal annealing in a continuous range of temperatures (T_{dd} = 70−120 °C) by using a Kofler bench, with the evolution of the charge transfer states tracked via IR spectroscopy and optical absorption spectroscopy (Figure S4).

Figures 1a and 1b show the evolution of the IR spectra after partially dedoping the polymer films. Here, for P3HT and
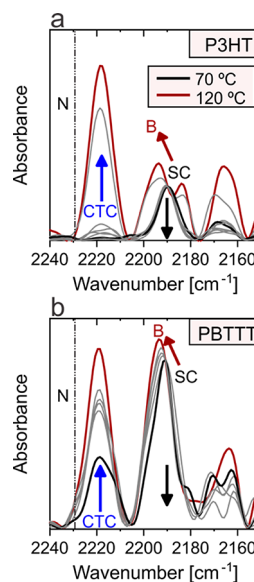
Figure 1. IR spectra for F4TCNQ-doped (a) P3HT and (b) PBTTT, centered on the −C≡N stretching region. In both cases, the data correspond to samples dedoped at equivalent temperatures and times (T_{dd} and t_{dd}, respectively, as labeled in (a)). Arrows indicate the evolution of each peak with increasing T_{dd}; the dashed line (N) indicates the position of neutral F4TCNQ. Data are normalized to the SC peak (2187 cm^{-1}), and background from polaron absorption is removed.

PBTTT, we see three peaks at 2194 cm^{-1} (B), 2187 cm^{-1} (SC), and 2170 cm^{-1} corresponding to the shifted −C≡N stretching modes for δ = 1, which for neutral F4TCNQ appear at 2227 cm^{-1} (N) and 2216 cm^{-1} (not resolved here). Moreover, Hase et al. reported a correlation between the dopant's location within the polymer network and the B and SC modes.[20] Their work suggested that B peaks correspond to dopant located within the backbone of the polymer while the SC peak was mostly affected by the placement of dopant within the side chains. In addition, their analysis highlighted the different stability behaviors for the dopant at each position.[20] For our experiments, both polymers show the presence of an additional peak at 2218 cm^{-1} (Figures 1a and 1b), which, according to eq 2, corresponds to a CTC with a δ = 0.2. We also see that for P3HT (Figure 1a) the SC mode
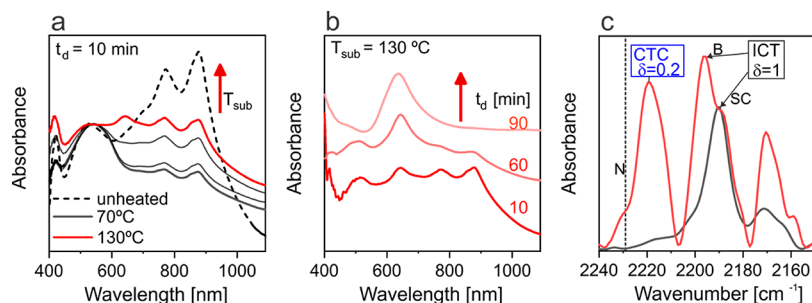
Figure 2. (a) Absorption spectra for PBTTT doped with F4TCNQ by using (a) fixed doping time t_d at various substrate temperatures T_{sub} and (b) fixed T_{sub} at various t_d. In (a), solid gray lines show the data for $T_{sub} = 70-130$ °C (bottom to top). The black dashed line corresponds to PBTTT conventionally doped by using an unheated substrate. Deep red curves represent the conditions depicted in the upcoming text as containing a "moderate CTC fraction" (c) IR spectra centered on the $-C\equiv N$ stretching region for PBTTT doped with F4TCNQ. The black curve corresponds to the unheated substrate. In (a) the data are normalized to the PBTTT NP transition while the data in (b) are normalized by thickness and offset for clarity due to the nearly absent NP transition at 90 min.

decreases in intensity upon heating while the feature at 2218 cm^{-1} (CTC) increases with temperature. For PBTTT (Figure 1b), the intensity of the CTC peak is clearly higher and at a similar ratio than the SC peak after annealing at 120 °C (contrary to P3HT). Also, there is a clear change in the ratio between the B and SC modes as a function of T_{dd}, which differs from the stability behavior previously seen in the literature.[20] Yet, it must be noted that doping protocols are different and, thus also, the final crystalline structure of the thin layer. Moreover, microscopy and thermoelectric analyses (Figures S5 and S6) show clear dedoping signs after thermal annealing, further evidencing different stability behaviors for the CTC and ICT states.

The above experiments show (i) that there are clear spectroscopic signatures of both ICT and CTC states in the maximally doped polymers and (ii) that temperature may be used to change the relative ratio between both doping mechanisms.

Recent experiments by Lim et al. indicated that doping from the vapor phase at elevated substrate temperatures can improve doping.[43] They identified that after using a t_d of 15 min, polymer substrate temperature (T_{sub}) in their setup reached 75−80 °C. They observed a linear increase in the alkyl- and π-stacking distance during in situ GIWAXS measurements for the temperatures reached during doping. This suggested an improved dopant diffusion through side chains caused by thermal expansion.[43] In their experiments, like in our initial tests, the substrate temperature was only indirectly "controlled" by the doping time. The doping vessel consisted of a 200 mL crystallization beaker with a Petri dish as the lid and sample holder while heating was done by placing the beaker on a hot plate at 210 °C, meaning that the lid could easily have reached 75−80 °C in the case of maximally doped samples. This suggests that a temperature-assisted vapor doping process can improve dopant diffusion and allow for a more controlled selection of the doping mechanism. Following this line of thought, we designed a more versatile setup, capable of independently controlling the temperatures of both the evaporation source and the substrate (instrumentation shown in Figure S3).

Hereafter, we analyze samples that were doped with controlled substrate temperature T_{sub}. Figure 2 shows the screening process of different doping conditions. The first approach (Figure 2a) consisted of increasing T_{sub} while keeping the doping time constant ($t_d = 10$ min). Here, we

observe an increase in the A$^-$ features up to $T_{sub} = 130$ °C before they drop again from 150 to 190 °C. We attribute the latter to simultaneous doping and dedoping (see Figure S6 and the discussion below).

In addition, the absorption feature at 640 nm is now well separated from the A$^-$ and NP bands, which unambiguously indicates that it belongs to CTC features observed by IR spectroscopy in Figure 1. Reassuringly, the electrical conductivity follows the same trend, reaching 85 S/cm at 130 °C and dropping to 28 S/cm at 190 °C (Table S2). Glass transition (T_g) and crystallization of the side chains in PBTTT occur at around 100 °C.[46] Hence, we rationalize these changes to come from three different effects. First, an increased T_{sub} avoids excessive dopant condensation on the polymer film surface, which would normally act as a "barrier" for the incoming dopant (see also micrographs in Figure S6 and the discussion below). Second, increased alkyl stacking distance due to thermal expansion improves diffusion through the polymer structure. Third, after thermal expansion (presumably from the side chains), inter- and intramolecular distances between dopant and host change, leading to changes in d as seen in other similar blends.[15]

Next, we evaluate the effect of different doping times ($t_d = 10$, 60, and 90 min) at a fixed substrate temperature ($T_{sub} = 130$ °C). Figure 2b shows that the CTC band increases while the A$^-$ features from the ICT and NP bands decrease before bleaching entirely at 90 min. Accordingly, the electrical conductivity drops from 85 to 3 S/cm (Table 1). These results are in line with the reports for P3HT and quater-thiophene.[13,17] As established in the literature, exciton dissociation of the ground state ICT readily occurs at room

Table 1. Dopant Fractions χ, Electrical Conductivity, and Seebeck Coefficient as a Function of Doping Conditions (Data Are Reported for the As-Doped Samples)

T_{sub}/t_d	χ_{CTC}	χ_{ICT}	electrical conductivity [S cm^{-1}]	Seebeck coefficient [μV K^{-1}]
nonheated/ 10 min	(low)		92	60 ± 3
130 °C/ 10 min	(moderate) 0.66	0.34	85	62 ± 4
130 °C/ 60 min	(high) 0.54	0.46	9	121 ± 14
130 °C/ 90 min	(maximum)		3	175 ± 31
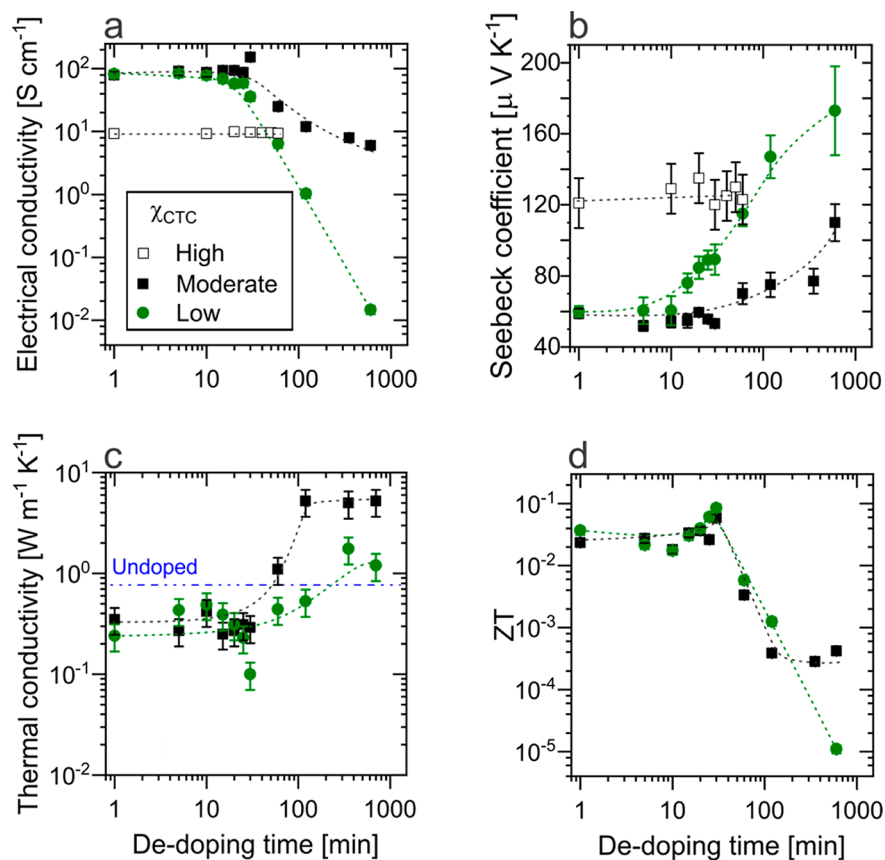
Figure 3. Thermoelectric properties of doped PBTTT films as a function of dedoping time at 100 °C: (a) electrical conductivity, (b) Seebeck coefficient, (c) thermal conductivity, and (d) figure of merit ZT. Samples with high, moderate, and low χ_{CTC} correspond to open black squares, solid black squares, and green circles, respectively. Dashed lines are a guide to the eye.

temperature,[8] whereas CTC can be considered charge neutral due to a higher binding energy.[10] In this sense, the drop in electrical conductivity comes from an interplay of CTC/ICT fractions, where each one has a different free charge carrier contribution.

Additional characterization using IR spectroscopy (Figure 2c) reveals a pronounced CTC peak. Here, the B mode is now visible and in a higher ratio than the SC mode. As these modes have been associated with dopant position with respect to the polymer, one may argue that temperature-assisted vapor doping results in dopant located at different places with respect to "conventional" vapor doping with uncontrolled substrate temperature (vide infra). Moreover, as in the work of Neelamraju et al., fitting of the IR spectra would suggest different coexisting charge-transfer states in *all* samples (Figure S7).[19] We thus infer that a low χ_{CTC} fraction is present even in samples doped by using an unheated substrate (Figure 2a, black dashed line), which then increases both with T_{sub} and t_d, reaching $\chi_{CTC} = 0.54$ when doped at 130 °C for 60 min (see Figure S7 and the related text for examples of how these fractions were obtained from spectroscopic data).

In line with the literature, increasing the χ_{CTC} within the total dopant content reduces the electrical conductivity. As stated before, although CTC is considered charge neutral,[10] some experiments were still able to measure small, nonzero values of σ for doped samples, even though no sign of ICT states was detected.[17] This suggests that carrier generation probably still occurs with further interaction from the present species, namely between neutral polymer and CTC.[11] Even

though this process is less efficient, it still contributes to the macroscopic conductivity with mobile charges. Most importantly, from Table 1 we see that keeping χ_{CTC} below a certain threshold level ($\chi_{CTC} \leq 0.34$) allows to maintain a comparatively high electrical conductivity.

Table 1 summarizes the estimated ICT and CTC fractions (χ) and the corresponding electrical conductivity and Seebeck coefficient values as a function of doping conditions for the previous sample set. For simplicity, "low", "moderate", "high", and "maximum" will be used in the following text to identify samples with the respective CTC content.

In this section, we have demonstrated that by controlling the substrate temperature and doping time, different ratios of CTC and ICT can be obtained. The fact that increased T_{sub} and t_d result in higher CTC content suggests that the two doping mechanisms may evolve differently if provided with enough energy, which in return can result in different stability trends. In the next section, we explore this interplay between the long-term stability of the thermoelectric properties and the CTC fraction.

3.2. Stability of the Thermoelectric Properties as a Function of CTC Content. While different binding energies have been presumed for the two doping mechanisms, there is little to no information about how stable these species are. Long-term stability is, however, crucial for thermoelectric applications. Research on heavier/bulkier dopants and the modification of polymer structures to increase molecular interactions are clear signs of its importance.[22,26] In the
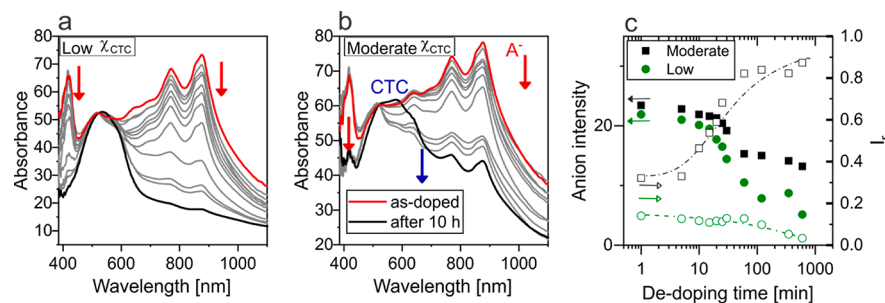
Figure 4. Absorption spectra of doped PBTTT films as a function of dedoping time at 100 °C for samples with (a) low and (b) moderate χ_{CTC}. (c) Peak intensity from fitted spectra and intensity ratio between peaks associated with CTC and anion bands as detailed in Figure S7. Arrows highlight the evolution of selected bands with increasing t_{dd}. Data are normalized at the NP transition for both samples.

following section, we explore the effect of χ_{CTC} on the thermal stability of PBTTT.

We have chosen to evaluate the stability of thermoelectric properties by measuring the change in electrical conductivity σ, Seebeck coefficient α, and thermal conductivity κ of doped PBTTT samples as a function of annealing time at elevated temperatures (in essence, an "accelerated aging" test). Annealing conditions were chosen on the premise that most dopant within the side chains leaves the polymer structure above 100 °C, while small time increments allow screening a full picture of the dedoping process.[20] Specifically, annealing conditions were set in two regimes: (i) T_{dd} = 100 °C and t_{dd} = 60 min in 10 min increments and (ii) extending the measurements to longer intervals of 1, 2, 5, and 10 h. In essence, this would allow visualizing both the intermediate and the extreme cases of the doped/dedoped polymer. During this section, we compare samples containing low, moderate, and high fractions of CTC states. Note also that although the selected dedoping temperature T_d = 100 °C is sufficiently close to the glass transition temperature of PBTTT, any concomitant morphological changes of the polymer itself are unlikely since all samples were precrystallized by thermal annealing prior to doping (see Materials and Methods section).

Figure 3 presents the thermoelectric properties of the three samples with different χ_{CTC}. The first noteworthy observation is that at the starting point samples containing low and moderate χ_{CTC} exhibit almost identical values of electrical conductivity, Seebeck coefficient, and thermal conductivity. This suggests that the ICT fraction is dominating the electrical transport properties of the different samples, and the corresponding microstructures are sufficiently similar to result in equivalent thermal conductivities.

As with previous experiments, electrical conductivity (Figure 3a) in the as-doped samples (t_{dd} = 0) yields nearly identical values of ~82 and 90 S/cm for samples with moderate and low χ_{CTC}, respectively. Then, after 10 h, σ drops to 6 and 0.01 S/cm for the samples with moderate and low χ_{CTC}, respectively. Interestingly, the sample containing a high χ_{CTC} fraction did not exhibit any degradation of its electrical conductivity for at least the measured period (60 min at 100 °C, see details in Figure S8), maintaining a value of ~9 S/cm. We draw attention to the fact that the σ value at which the sample with a moderate CTC saturates coincides with the σ value for the sample with a high χ_{CTC}. This match strongly suggests that CTC is a much more stable state than ICT under thermal stress and that the drop in conductivity observed for the moderate χ_{CTC} sample is due to loss of the ICT (see also next section). Interestingly, thicker samples also show the same

trend: ICT is less stable than CTC (Figure S8), which would suggest that this is indeed a fundamental effect occurring within the bulk of the film affecting the two doping mechanisms for the F4TCNQ/PBTTT system.

The Seebeck coefficient α follows an opposite trend to σ (Figure 3b): starting at 60 μV K^{-1} and changing to 90 and 53 μV K^{-1} after 30 min for the samples with low and moderate χ_{CTC}, respectively. Then, after 10 h, α increases in both series up to 173 and 110 μV K^{-1} for the low and moderate χ_{CTC} cases, respectively. These values agree with the final higher electrical conductivities found in samples that originally had higher χ_{CTC}.

Interestingly, the thermal conductivity κ of the as-doped samples in the same set (Figure 3c) starts at lower values (~0.3 W m^{-1} K^{-1}) than the reference undoped PBTTT (~0.8 W m^{-1} K^{-1}). This is likely due to a scattering effect for thermal transport induced by the interdiffusion of the large molecular dopants and/or changes in the degree of crystallinity upon doping (see next section). An in-depth study of the scattering mechanisms will be the topic of a future work, as it goes beyond the scope of the present piece. The thermal conductivity values do not change significantly during the first 30 min of annealing but then begin to increase, finally reaching values of around 1 and 5 W m^{-1} K^{-1} for samples with low and moderate χ_{CTC}, respectively. The significant drop in electrical conductivity within the same range (t_{dd} = 2, 5, and 10 h) indicates a much lower number of charge carriers for those samples compared to the as-doped which, following the Wiedemann–Franz law, implies that the increase in κ is not due to the electronic contribution of the thermal conductivity but rather the lattice one (Figure S9). The similar κ values for the undoped PBTTT reference and the highly dedoped samples (t_{dd} = 2, 5, and 10 h) with low χ_{CTC} suggest that these samples are structurally similar to the reference. As we will see below, the larger κ (5 W m^{-1} K^{-1}) for strongly dedoped sample with initial moderate χ_{CTC} is likely to be due to the formation of F4TCNQ crystals on the surface of the sample upon continued thermal stress.

Figure 3d combines these results into ZT values for both series which after 30 min (t_{dd}) show peak values of 0.08 and 0.05 for the low and moderate χ_{CTC} cases, respectively. Here, the evolution of highly dedoped samples (t_{dd} = 10 h) shows ZT values of 1 × 10^{-5} and 4 × 10^{-4} for the low and moderate χ_{CTC} cases. Although the electrical conductivity decreases in both cases, the samples with moderate χ_{CTC} are more stable, as expected, even when taking into account the (probably overestimated) high thermal conductivity. A more realistic
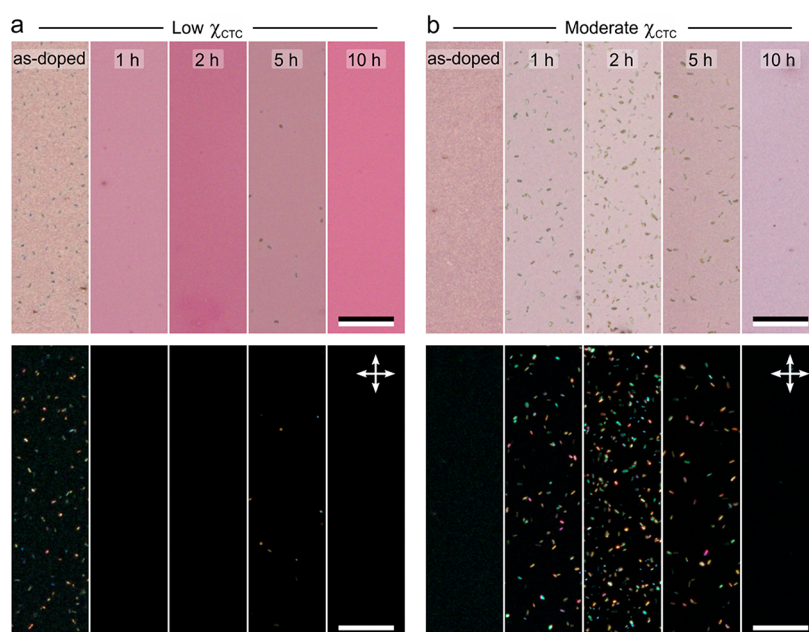
Figure 5. Transmitted-light microscopy for the (a) low and (b) moderate χ_{CTC} series, showing PBTTT films as a function of dedoping time (as indicated). Unpolarized (top row) and cross-polarized (bottom row) micrographs are shown. Constant imaging settings were used. Scale bar = 50 μm.
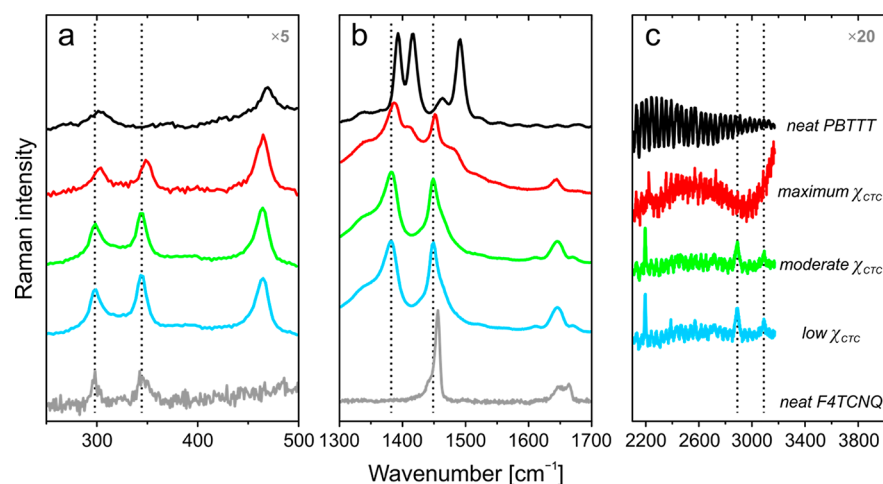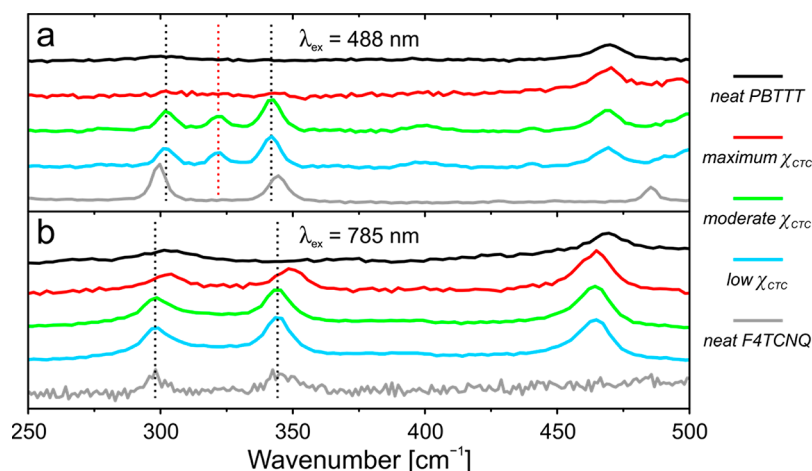

Figure 6. Raman spectra of doped PBTTT samples with different χ_{CTC} content as well as reference spectra of undoped/neat PBTTT and neutral F4TCNQ (as indicated). Panels a−c show different spectral regions. Vertical dotted markers indicate selected peak positions for the samples with low/moderate χ_{CTC}. Excitation wavelength λ_{ex} = 785 nm; spectra are peak-normalized for clarity. The data in (a) and (c) are magnified ×5 and ×20, respectively.

ZT estimate (correcting for κ) for the moderate χ_{CTC} case after 10 h would be 0.002 (cf. 1×10^{-5} for the low χ_{CTC} case).

3.3. Correlation of Stability and Doping Mechanism by Spectroscopic and Structural Characterization. To further understand the thermal stability of these samples, additional characterization was performed. Figure 4 shows the evolution of the optical absorption spectra upon continuous annealing for two samples featuring low and moderate χ_{CTC}. Here, both series show clear signs of dedoping as the absorption spectra tend toward the shape of the undoped pristine film. Nonetheless, the A$^-$ and CTC bands are still present at the end of the experiment (black curve, after 10 h) in samples with moderate χ_{CTC} (as opposed to the low χ_{CTC} case) and exemplified in the peak analysis in Figure 4c and Figure S7. For thicker samples, it is very clearly observed how

the peaks associated with the ICT (A$^-$) are quenched much faster than those associated with the CTC (Figure S8). This indicates that the rate of depletion of ICT state dopants is substantially faster than that of CTC state dopants. In the following, we try to assess whether this is due to the dopant being situated in different locations with respect to the polymer or, alternatively, is a result of a larger binding energy for the dopant to the polymer.

Optical microscopy (Figure 5) corroborates the differences in doping stability between the two sets. Here, the as-doped samples with a low χ_{CTC} (Figure 5a) show a considerable amount of F4TCNQ crystals on the surface, previously suggested to have a detrimental effect on doping by acting as a "barrier" for the incoming dopant during processing. These crystals are particularly well detected by using cross-polarized

Figure 7. Raman spectra of doped PBTTT samples with different χ_{CTC} content as well as reference spectra of undoped/neat PBTTT and neutral F4TCNQ (as indicated), showing an expanded view of the $250-500$ cm^{-1} spectral region. Spectra were recorded with excitation at (a) 488 nm and (b) 785 nm. Vertical dotted markers indicate selected peak positions for the samples with low/moderate χ_{CTC}. Data are peak-normalized in the $1380-1460$ cm^{-1} region (as in Figure 6).

microscopy. Interestingly, they disappear entirely after 1 h. On the other hand, the as-doped samples with a moderate χ_{CTC} (Figure 5b) show no visible dopant crystals on the film surface, presumably due to the fabrication method that employs longer deposition times at temperatures above F4TCNQ sublimation. Then, following postannealing, dopant crystals emerge from the polymer network onto the surface ($t_{dd} = 1$, 2, and 5 h) before finally disappearing at the final step ($t_{dd} = 10$ h). These crystals may be responsible for the increase in thermal conductivity after long thermal stress, as measured by frequency-domain thermoreflectance (Figure 3c).

Also noteworthy are the changes in color upon dedoping. Here, for samples with a low χ_{CTC}, a rapid recovery of the pink color of pristine PBTTT can be seen due to pronounced dedoping and re-emergence of the absorption band of neutral PBTTT (Figure 5a). On the other hand, the series with moderate χ_{CTC} (Figure 5b) shows a more gradual change, consistent with the higher thermal stability of doping, with the emergence of pink color seen only after 10 h. Hence, both absorption and optical microscopy analyses confirm that samples featuring a moderate/high χ_{CTC} are thermally more stable than samples dominated by the ICT doping mechanism.

Through our previous experiments, we have shown that the presence of CTC states within the total doped content improves the long-term stability. Moreover, our IR analysis suggests that the processing conditions that lead to increased χ_{CTC} are also accompanied by the emergence of vibrational modes associated with the dopant allocated within the polymer backbone, suggesting changes in morphology similar to those reported for codeposition techniques. These results motivate us to further analyze the structural changes of the polymer network.

3.4. Raman Spectroscopy. Figure 6 shows the Raman spectra of three representative samples with low, moderate, and maximum χ_{CTC} as well as that of the neat (undoped) PBTTT and F4TCNQ references. The central region of the spectrum centered at ~1500 cm^{-1} (Figure 6b) corresponds to vibrations related to the backbone of the polymer, mainly carbon single/double bonds symmetric/asymmetric stretching/bending modes. Accordingly, these vibrations localized in the conjugated core are strongly affected by the generated carriers which navigate through the π-system. As a result, the

peak shifts follow the differences in conductivity between the samples, from the film with higher conductivity (low χ_{CTC}) toward the reference undoped PBTTT film.

Higher energy vibrations (around $2500-3200$ cm^{-1}) are typically related to modes involving lighter atoms, such as the C−H stretching vibrations. In Figure 6c, we examine two modes centered at 2890 and 3090 cm^{-1} which are assigned to C−H$_2$ stretching and aromatic C−H stretching, respectively.[47] The weaker 3090 cm^{-1} mode cannot be well resolved in all samples due to variations in the signal-to-noise ratio in the data. However, the more intense 2890 cm^{-1} mode belonging to the tetradecyl side chains of PBTTT is only observed for samples with low/moderate CTC content while being absent for the sample with maximum χ_{CTC} as well as the reference PBTTT film. The latter suggests that the side-chain packing for the sample with maximum χ_{CTC} closely matches that of the undoped polymer, implying that in the CTC state the dopant is unlikely to be located in the vicinity of the side chains. On the other hand, the appearance of the 2890 cm^{-1} mode for samples with low/moderate χ_{CTC} indicates that the side-chain packing of the polymer is altered,[48] from which we infer that the dopant molecules forming the ICT state are indeed preferentially located around the side chains, in agreement with the IR data (Figure 2c). Therefore, besides possible differences for CTC and ICT in the dopant−polymer binding energy, dopants are, at least partially, located in different parts of the film.

Finally, low-energy vibrations (centered at a few hundred cm^{-1}) are associated with either vibrations involving heavy atoms or vibrations extended over a larger group of atoms. This is, for instance, the region where signatures of different polymorphs are often observed. Given that the studied materials do not include heavy atoms, the spectral changes in this region are thus interpreted in terms of variations in polymer/dopant microstructure. Figure 6a shows, along with the above-discussed softening of the PBTTT-related peak, the emergence of two strong peaks at ~298 and 344 cm^{-1}. By inspection of the reference spectra, it is clear that these peaks are related to F4TCNQ, with their enhancement ascribed to the effect of excitation at 785 nm being resonant with the absorption of F4TCNQ radical anions (see Figure 2a). It is worth noting that these peaks exhibit a 5 cm^{-1} shift to higher
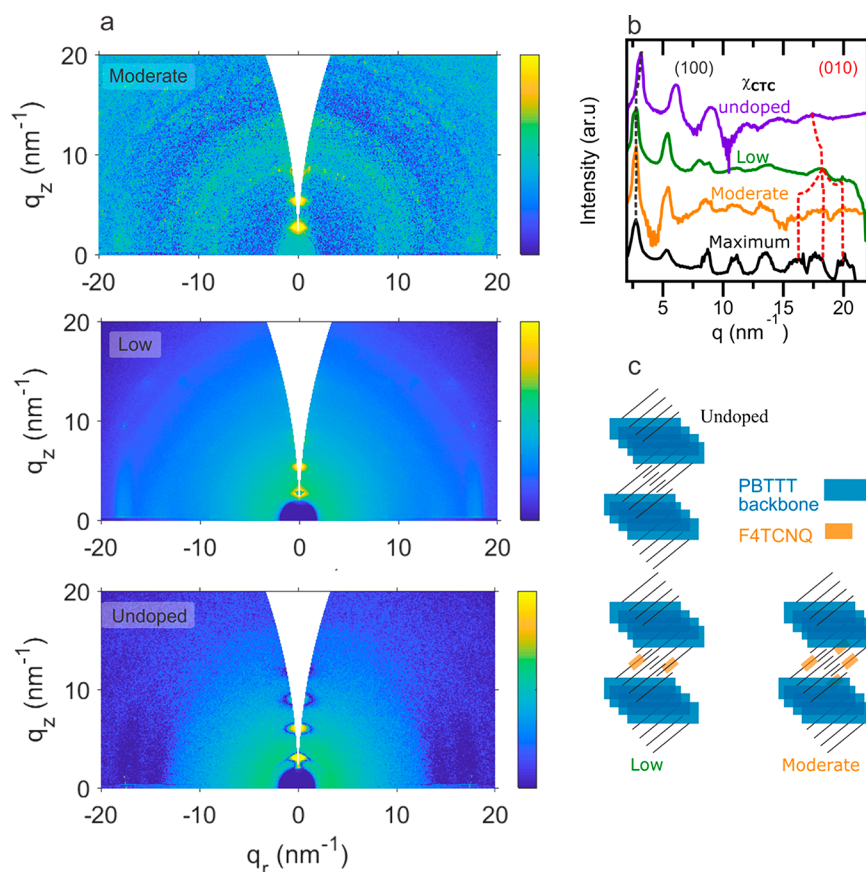
Figure 8. (a) 2D GIWAXS patterns for selected samples. (b) Large integrated patterns for the same samples as in the left panel as well for that with maximal χ_{CTC}. (c) Sketch of suggested dopant position with increased CTC content.

energies for the sample with maximum χ_{CTC} relative to the samples with low/moderate χ_{CTC}. This is indicative of (i) increased intermolecular interactions for the CTC state and (ii) preferential placement of the corresponding dopant within the crystalline polymer fraction of PBTTT given that here the excitation is also preresonant with the absorption of crystalline PBTTT.

A natural extension of the analysis above is to compare Raman spectra recorded with different excitation wavelengths, λ_{ex}, which, by virtue of resonant enhancement, would preferentially select different species within the doped samples. Figure 7 shows Raman spectra for the same samples and spectral region as in Figure 6a recorded with excitation at 785 nm (as above; preferentially exciting F4TCNQ anions and crystalline PBTTT) and 488 nm (preferentially exciting amorphous PBTTT). As before, we focus on the peaks at ~300 and 340 cm^{-1}. Comparison of the data obtained with the two different excitations shows that, remarkably, these peaks are entirely absent for the maximum χ_{CTC} sample for $\lambda_{ex} = 488$ nm (unlike for $\lambda_{ex} = 785$ nm; cf. Figures 7a and 7b), corroborating the proposal that the CTC state dopant is indeed located primarily within crystalline PBTTT regions. Conversely, a new peak is seen at 322 cm^{-1} for samples with low/moderate χ_{CTC} for $\lambda_{ex} = 488$ nm which is absent in the $\lambda_{ex} = 785$ nm data. Although its origin is unclear, the contrast with the maximum χ_{CTC} sample nevertheless allows us to propose that the ICT state is formed by dopants located primarily within the amorphous/interstitial regions of the polymer network.

3.5. Grazing-Incidence Wide-Angle X-ray Scattering (GIWAXS).

To further investigate the changes in the crystalline part, we have analyzed the samples using GIWAXS. X-ray scattering has been recently coupled with FTIR experiments to deduce dopant position within host/dopant systems,[20] revealing, in the case of P3HT, that doping generally modifies the spacing between (h00) crystalline planes (associated with the lamellar packing of aromatic backbones and aliphatic side chains) and ($0k0$) crystalline planes (associated with the $\pi-\pi$ stacking).

Specifically, five changes have been observed and correlated to other optical and/or electrical properties. (1) First, low dopant content diffuses primarily into the amorphous regions, which does not influence directly the scattering patterns but changes significantly the electrical conductivity. (2) Increasing the dopant content broadens scattering features but does not contribute to any particular shift or new peaks. (3) Further increase in the dopant content shifts the (100) peak toward lower q, indicating an expansion of the lamellar packing. (4) The ($0k0$) peaks attributed to the $\pi-\pi$ stacking, e.g. (010), shift to higher q, indicating a contraction of the lattice in that direction. (5) Finally, in high dopant content regimes, the (010) reflection splits into new patterns, which has been associated with mixed crystalline phases with different tilting angles of the polymer backbone. It has also been attributed to the intercalation of dopant between the polymer backbones and the formation of dopant/polymer cocrystals.[19,43,49−51] PBTTT proceeds in a similar fashion, yet to our knowledge, there are no literature reports that show patterns as those indicating mixed crystalline phases in the (010) orientation.

Our GIWAXS patterns, shown in Figure 8, mostly agree with previously reported studies.[35,51] A detailed analysis of these GIWAXS patterns including the position (i.e., the Q value) and fwhm of the diffraction peaks as well as the corresponding d-spacing is provided in Table 2. Our results confirm a reduction

Table 2. Summarized Data from GIWAXS Patterns

	(100)			(010)	
	Q (peak max, nm^{-1})	fwhm (nm^{-1})	d-spacing (nm)	Q (Peak max, nm^{-1})	d-spacing (nm)
pristine PBTTT					
annealed	3.1	0.42	2.03	17.4	0.36
nonannealed	3.16	0.29	1.99	17.4	0.36
doped PBTTT					
low χ_{CTC}	2.84	0.41	2.12	18	0.35
moderate χ_{CTC}	2.8	0.19	2.24		
max χ_{CTC}	2.76	0.33	2.28	17.9	0.35

of the $\pi-\pi$ stacking distance and an increase of the lamellar packing distance upon doping the polymer (Figure 8b, dotted lines). Additionally, we see the appearance of new peaks in the typical Q-region where the (010) shows up for the samples with moderate and maximum χ_{CTC} (Figure 8b). However, these features are partially masked by the appearance of peaks associated with neutral F4TCNQ crystals both on the surface and within the polymer, which increase with increased doping time (please refer to Figure S10 for the all GIWAXS patterns as a function of doping conditions). Therefore, in agreement with the Raman spectra at low energies, the crystalline structure of the PBTTT is distorted a little by the ICT and more strongly when the CTC fraction increases (see Table 2).

These distortions of the molecular packing are compatible with the positioning of the dopant molecules within interstitial regions between aromatic backbones. The fact that the samples with increased CTC content show a decreased intensity in the SC peak in IR (compared to B), or the high-energy Raman peaks (Figure 6c), might be related to (i) spectroscopy preferentially probing amorphous domains or (ii) CTC and ICT forming different polymorphs or cocrystals. The appearance of new peaks in the GIWAXS data supports the second option.

4. CONCLUSIONS

We have established a doping method to obtain a desired CTC to ICT fraction. The method relies on controlling the temperature of the substrate during evaporation of the dopant. This enabled us to assess the role of different CTC fractions in doped PBTTT films in terms of their thermoelectric properties, namely, the electrical conductivity, Seebeck coefficient, and thermal conductivity. Moreover, we followed the thermal stability of the thermoelectric parameters upon continuous exposure to 100 °C for ca. 10 h. We found that samples rich in CTC are more thermally stable than those based on higher ICT fractions. Interestingly, samples exhibiting intermediate CTC fractions result simultaneously in good thermoelectric properties and improved stability. To understand this, we performed a combined study including absorption, polarized optical microscopy, Raman spectroscopy, and GIWAXS. The resulting structural picture is that dopant

molecules leading to CTC preferentially affect the crystalline domains, thus being locked within the crystal structure.

■ ASSOCIATED CONTENT

⑤ Supporting Information
The Supporting Information is available free of charge at https://pubs.acs.org/doi/10.1021/acs.macromol.9b02263.

Summary of organic systems and reported doping mechanisms, experimental setup, absorption spectra of doped P3HT and PBTTT, experimental setup with added heating elements, absorption and IR spectra of doped PBTTT, Seebeck coefficient and electrical conductivity measurements, micrographs of doped P3HT, electrical conductivity of doped PBTTT as a function of T_{sub}, peak fitting of IR and absorption spectra, absorption spectra of dedoped PBTTT, estimated electrical conductivity and thermal conductivity and GIWAXS patterns with selected processing conditions (PDF)

■ AUTHOR INFORMATION

Corresponding Author
*E-mail mcampoy@icmab.es, m.campoy@csic.es.

ORCID ⓘ
Osnat Zapata-Arteaga: 0000-0002-0844-2773
Aleksandr Perevedentsev: 0000-0003-0146-3560
Jaime Martín: 0000-0002-9669-7273
Mariano Campoy-Quiles: 0000-0002-8911-640X

Notes
The authors declare no competing financial interest.

■ REFERENCES

(1) Wang, H.; Yu, C. Organic Thermoelectrics: Materials Preparation, Performance Optimization, and Device Integration. *Joule* **2019**, *3* (1), 53−80.

(2) Bubnova, O.; Khan, Z. U.; Malti, A.; Braun, S.; Fahlman, M.; Berggren, M.; Crispin, X. Optimization of the Thermoelectric Figure of Merit in the Conducting Polymer Poly(3,4-Ethylenedioxythiophene). *Nat. Mater.* **2011**, *10* (6), 429−433.

(3) Kar, P. *Doping in Conjugated Polymers*; John Wiley & Sons, Inc.: Hoboken, NJ, 2013.

(4) Lüssem, B.; Riede, M.; Leo, K. Doping of Organic Semiconductors. *Phys. Status Solidi A* **2013**, *210* (1), 9−43.

(5) Salzmann, I.; Heimel, G.; Duhm, S.; Oehzelt, M.; Pingel, P.; George, B. M.; Schnegg, A.; Lips, K.; Blum, R.-P.; Vollmer, A.; et al. Intermolecular Hybridization Governs Molecular Electrical Doping. *Phys. Rev. Lett.* **2012**, *108* (3), 035502.

(6) Kiefer, D.; Kroon, R.; Hofmann, A. I.; Sun, H.; Liu, X.; Giovannitti, A.; Stegerer, D.; Cano, A.; Hynynen, J.; Yu, L.; et al. Double Doping of Conjugated Polymers with Monomer Molecular Dopants. *Nat. Mater.* **2019**, *18* (2), 149−155.

(7) Li, J.; Duchemin, I.; Roscioni, O. M.; Friederich, P.; Anderson, M.; Da Como, E.; Kociok-Köhn, G.; Wenzel, W.; Zannoni, C.; Beljonne, D.; et al. Host Dependence of the Electron Affinity of Molecular Dopants. *Mater. Horiz.* **2019**, *6* (1), 107−114.

(8) Tietze, M. L.; Benduhn, J.; Pahner, P.; Nell, B.; Schwarze, M.; Kleemann, H.; Krammer, M.; Zojer, K.; Vandewal, K.; Leo, K. Elementary Steps in Electrical Doping of Organic Semiconductors. *Nat. Commun.* **2018**, *9* (1), 1182.

(9) Jacobs, I. E.; Moulé, A. J. Controlling Molecular Doping in Organic Semiconductors. *Adv. Mater.* **2017**, *29* (42), 1703063.

(10) Salzmann, I.; Heimel, G.; Oehzelt, M.; Winkler, S.; Koch, N. Molecular Electrical Doping of Organic Semiconductors: Fundamental Mechanisms and Emerging Dopant Design Rules. *Acc. Chem. Res.* **2016**, *49* (3), 370−378.

(11) Pingel, P.; Neher, D. Comprehensive Picture of P-Type Doping of P3HT with the Molecular Acceptor F4TCNQ. *Phys. Rev. B: Condens. Matter Mater. Phys.* **2013**, *87* (11), 115209.

(12) Enokida, I.; Furukawa, Y. Doping-Level Dependent Mobilities of Positive Polarons and Bipolarons in Poly(2,5-Bis(3-Hexadecylthiophen-2-Yl)Thieno[3,2-b]Thiophene) (PBTTT-C16) Based on an Ionic-Liquid-Gated Transistor Configuration. *Org. Electron.* **2019**, *68*, 28−34.

(13) Méndez, H.; Heimel, G.; Winkler, S.; Frisch, J.; Opitz, A.; Sauer, K.; Wegner, B.; Oehzelt, M.; Röthel, C.; Duhm, S.; et al. Charge-Transfer Crystallites as Molecular Electrical Dopants. *Nat. Commun.* **2015**, *6*, 8560.

(14) Coropceanu, V.; Cornil, J.; da Silva Filho, D. A.; Olivier, Y.; Silbey, R.; Brédas, J.-L. Charge Transport in Organic Semiconductors. *Chem. Rev.* **2007**, *107* (4), 926−952.

(15) Hu, P.; Wang, S.; Chaturvedi, A.; Wei, F.; Zhu, X.; Zhang, X.; Li, R.; Li, Y.; Jiang, H.; Long, Y.; et al. Impact of C−H⋯X (X = F, N) and π−π Interactions on Tuning the Degree of Charge Transfer in F6TNAP-Based Organic Binary Compound Single Crystals. *Cryst. Growth Des.* **2018**, *18* (3), 1776−1785.

(16) Zhu, L.; Kim, E.-G.; Yi, Y.; Brédas, J.-L. Charge Transfer in Molecular Complexes with 2,3,5,6-Tetrafluoro-7,7,8,8-Tetracyanoquinodimethane (F4TCNQ): A Density Functional Theory Study. *Chem. Mater.* **2011**, *23* (23), 5149−5159.

(17) Jacobs, I. E.; Cendra, C.; Harrelson, T. F.; Bedolla Valdez, Z. I.; Faller, R.; Salleo, A.; Moulé, A. J. Polymorphism Controls the Degree of Charge Transfer in a Molecularly Doped Semiconducting Polymer. *Mater. Horiz.* **2018**, *5* (4), 655−660.

(18) Valencia, A. M.; Cocchi, C. Electronic and Optical Properties of Oligothiophene-F4TCNQ Charge-Transfer Complexes: The Role of the Donor Conjugation Length. *J. Phys. Chem. C* **2019**, *123* (14), 9617−9623.

(19) Neelamraju, B.; Watts, K. E.; Pemberton, J. E.; Ratcliff, E. L. Correlation of Coexistent Charge Transfer States in F4TCNQ-Doped P3HT with Microstructure. *J. Phys. Chem. Lett.* **2018**, *9* (23), 6871−6877.

(20) Hase, H.; O'Neill, K.; Frisch, J.; Opitz, A.; Koch, N.; Salzmann, I. Unraveling the Microstructure of Molecularly Doped Poly(3-Hexylthiophene) by Thermally Induced Dedoping. *J. Phys. Chem. C* **2018**, *122* (45), 25893−25899.

(21) Liu, J.; Qiu, L.; Portale, G.; Koopmans, M.; ten Brink, G.; Hummelen, J. C.; Koster, L. J. A. N-Type Organic Thermoelectrics: Improved Power Factor by Tailoring Host-Dopant Miscibility. *Adv. Mater.* **2017**, *29* (36), 1701641.

(22) Kroon, R.; Kiefer, D.; Stegerer, D.; Yu, L.; Sommer, M.; Müller, C. Polar Side Chains Enhance Processability, Electrical Conductivity, and Thermal Stability of a Molecularly p-Doped Polythiophene. *Adv. Mater.* **2017**, *29* (24), 1700930.

(23) Li, J.; Zhang, G.; Holm, D. M.; Jacobs, I. E.; Yin, B.; Stroeve, P.; Mascal, M.; Moulé, A. J. Introducing Solubility Control for Improved Organic P-Type Dopants. *Chem. Mater.* **2015**, *27* (16), 5765−5774.

(24) Scholes, D. T.; Yee, P. Y.; McKeown, G. R.; Li, S.; Kang, H.; Lindemuth, J. R.; Xia, X.; King, S. C.; Seferos, D. S.; Tolbert, S. H.; et al. Designing Conjugated Polymers for Molecular Doping: The Roles of Crystallinity, Swelling, and Conductivity in Sequentially-Doped Selenophene-Based Copolymers. *Chem. Mater.* **2019**, *31* (1), 73−82.

(25) Koech, P. K.; Padmaperuma, A. B.; Wang, L.; Swensen, J. S.; Polikarpov, E.; Darsell, J. T.; Rainbolt, J. E.; Gaspar, D. J. Hexafluorotetracyanonaphthoquinodimethane (F6-TNAP): A Conductivity Dopant for Organic Light-Emitting Devices. *Chem. Mater.* **2010**, *22* (8), 3926−3932.

(26) Li, J.; Rochester, C. W.; Jacobs, I. E.; Friedrich, S.; Stroeve, P.; Riede, M.; Moulé, A. J. Measurement of Small Molecular Dopant F4TCNQ and C 60 F 36 Diffusion in Organic Bilayer Architectures. *ACS Appl. Mater. Interfaces* **2015**, *7* (51), 28420−28428.

(27) Goetz, K. P.; Vermeulen, D.; Payne, M. E.; Kloc, C.; McNeil, L. E.; Jurchescu, O. D. Charge-Transfer Complexes: New Perspectives on an Old Class of Compounds. *J. Mater. Chem. C* **2014**, *2* (17), 3065−3076.

(28) Li, J.; Rochester, C. W.; Jacobs, I. E.; Aasen, E. W.; Friedrich, S.; Stroeve, P.; Moulé, A. J. The Effect of Thermal Annealing on Dopant Site Choice in Conjugated Polymers. *Org. Electron.* **2016**, *33*, 23−31.

(29) Müller, L.; Rhim, S.-Y.; Sivanesan, V.; Wang, D.; Hietzschold, S.; Reiser, P.; Mankel, E.; Beck, S.; Barlow, S.; Marder, S. R.; et al. Electric-Field-Controlled Dopant Distribution in Organic Semiconductors. *Adv. Mater.* **2017**, *29* (30), 1701466.

(30) Andersson, M. R.; Thomas, O.; Mammo, W.; Svensson, M.; Theander, M.; Inganäs, O. Substituted Polythiophenes Designed for Optoelectronic Devices and Conductors. *J. Mater. Chem.* **1999**, *9* (9), 1933−1940.

(31) Liu, J.; Qiu, L.; Portale, G.; Torabi, S.; Stuart, M. C. A.; Qiu, X.; Koopmans, M.; Chiechi, R. C.; Hummelen, J. C.; Anton Koster, L. J. Side-Chain Effects on N-Type Organic Thermoelectrics: A Case Study of Fullerene Derivatives. *Nano Energy* **2018**, *52*, 183−191.

(32) Jacobs, I. E.; Aasen, E. W.; Oliveira, J. L.; Fonseca, T. N.; Roehling, J. D.; Li, J.; Zhang, G.; Augustine, M. P.; Mascal, M.; Moulé, A. J. Comparison of Solution-Mixed and Sequentially Processed P3HT:F4TCNQ Films: Effect of Doping-Induced Aggregation on Film Morphology. *J. Mater. Chem. C* **2016**, *4* (16), 3454−3466.

(33) Jacobs, I. E.; Aasen, E. W.; Nowak, D.; Li, J.; Morrison, W.; Roehling, J. D.; Augustine, M. P.; Moulé, A. J. Direct-Write Optical Patterning of P3HT Films Beyond the Diffraction Limit. *Adv. Mater.* **2017**, *29* (2), 1603221.

(34) Kang, K.; Watanabe, S.; Broch, K.; Sepe, A.; Brown, A.; Nasrallah, I.; Nikolka, M.; Fei, Z.; Heeney, M.; Matsumoto, D.; et al. 2D Coherent Charge Transport in Highly Ordered Conducting Polymers Doped by Solid State Diffusion. *Nat. Mater.* **2016**, *15* (8), 896−902.

(35) Patel, S. N.; Glaudell, A. M.; Peterson, K. A.; Thomas, E. M.; O'Hara, K. A.; Lim, E.; Chabinyc, M. L. Morphology Controls the Thermoelectric Power Factor of a Doped Semiconducting Polymer. *Sci. Adv.* **2017**, *3* (6), e1700434.

(36) Hamidi-Sakr, A.; Biniek, L.; Bantignies, J.-L.; Maurin, D.; Herrmann, L.; Leclerc, N.; Lévêque, P.; Vijayakumar, V.; Zimmermann, N.; Brinkmann, M. A Versatile Method to Fabricate Highly In-Plane Aligned Conducting Polymer Films with Anisotropic Charge Transport and Thermoelectric Properties: The Key Role of Alkyl Side Chain Layers on the Doping Mechanism. *Adv. Funct. Mater.* **2017**, *27* (25), 1700173.

(37) Fujimoto, R.; Yamashita, Y.; Kumagai, S.; Tsurumi, J.; Hinderhofer, A.; Broch, K.; Schreiber, F.; Watanabe, S.; Takeya, J. Molecular Doping in Organic Semiconductors: Fully Solution-

Processed, Vacuum-Free Doping with Metal−Organic Complexes in an Orthogonal Solvent. *J. Mater. Chem. C* **2017**, *5* (46), 12023−12030.

(38) Patel, S. N.; Glaudell, A. M.; Kiefer, D.; Chabinyc, M. L. Increasing the Thermoelectric Power Factor of a Semiconducting Polymer by Doping from the Vapor Phase. *ACS Macro Lett.* **2016**, *5* (3), 268−272.

(39) Jacobs, I. E.; Wang, F.; Hafezi, N.; Medina-Plaza, C.; Harrelson, T. F.; Li, J.; Augustine, M. P.; Mascal, M.; Moulé, A. J. Quantitative Dedoping of Conductive Polymers. *Chem. Mater.* **2017**, *29* (2), 832−841.

(40) Fuzell, J.; Jacobs, I. E.; Ackling, S.; Harrelson, T. F.; Huang, D. M.; Larsen, D.; Moulé, A. J. Optical Dedoping Mechanism for P3HT:F4TCNQ Mixtures. *J. Phys. Chem. Lett.* **2016**, *7* (21), 4297−4303.

(41) Zuo, G.; Andersson, O.; Abdalla, H.; Kemerink, M. High Thermoelectric Power Factor from Multilayer Solution-Processed Organic Films. *Appl. Phys. Lett.* **2018**, *112*, 083303.

(42) Hynynen, J.; Kiefer, D.; Yu, L.; Kroon, R.; Munir, R.; Amassian, A.; Kemerink, M.; Müller, C. Enhanced Electrical Conductivity of Molecularly P-Doped Poly(3-Hexylthiophene) through Understanding the Correlation with Solid-State Order. *Macromolecules* **2017**, *50* (20), 8140−8148.

(43) Lim, E.; Peterson, K. A.; Su, G. M.; Chabinyc, M. L. Thermoelectric Properties of Poly(3-Hexylthiophene) (P3HT) Doped with 2,3,5,6-Tetrafluoro-7,7,8,8-Tetracyanoquinodimethane (F4TCNQ) by Vapor-Phase Infiltration. *Chem. Mater.* **2018**, *30* (3), 998−1010.

(44) Dixon, D. A.; Calabrese, J. C.; Miller, J. S. Crystal and Molecular Structure of the 2:1 Charge-Transfer Salt of Decamethyl-ferrocene and Perfluoro-7,7,8,8-Tetracyano-p-Quinodimethane: [[Fe-(C5Me5)2]+.]2[TCNQF4]2-. The Electronic Structure of [TCNQF4]n (n = 0, 1-, 2-). *J. Phys. Chem.* **1989**, *93* (6), 2284−2291.

(45) Schmidt, A. J.; Cheaito, R.; Chiesa, M. A Frequency-Domain Thermoreflectance Method for the Characterization of Thermal Properties. *Rev. Sci. Instrum.* **2009**, *80* (9), 094901.

(46) Root, S. E.; Alkhadra, M. A.; Rodriquez, D.; Printz, A. D.; Lipomi, D. J. Measuring the Glass Transition Temperature of Conjugated Polymer Films with Ultraviolet−Visible Spectroscopy. *Chem. Mater.* **2017**, *29* (7), 2646−2654.

(47) Corsetti, S.; Rabl, T.; McGloin, D.; Kiefer, J. Intermediate Phases during Solid to Liquid Transitions in Long-Chain n-Alkanes. *Phys. Chem. Chem. Phys.* **2017**, *19* (21), 13941−13950.

(48) Miller, N. C.; Sweetnam, S.; Hoke, E. T.; Gysel, R.; Miller, C. E.; Bartelt, J. A.; Xie, X.; Toney, M. F.; McGehee, M. D. Molecular Packing and Solar Cell Performance in Blends of Polymers with a Bisadduct Fullerene. *Nano Lett.* **2012**, *12* (3), 1566−1570.

(49) Scholes, D. T.; Hawks, S. A.; Yee, P. Y.; Wu, H.; Lindemuth, J. R.; Tolbert, S. H.; Schwartz, B. J. Overcoming Film Quality Issues for Conjugated Polymers Doped with F 4 TCNQ by Solution Sequential Processing: Hall Effect, Structural, and Optical Measurements. *J. Phys. Chem. Lett.* **2015**, *6* (23), 4786−4793.

(50) Duong, D. T.; Wang, C.; Antono, E.; Toney, M. F.; Salleo, A. The Chemical and Structural Origin of Efficient P-Type Doping in P3HT. *Org. Electron.* **2013**, *14* (5), 1330−1336.

(51) Cochran, J. E.; Junk, M. J. N.; Glaudell, A. M.; Miller, P. L.; Cowart, J. S.; Toney, M. F.; Hawker, C. J.; Chmelka, B. F.; Chabinyc, M. L. Molecular Interactions and Ordering in Electrically Doped Polymers: Blends of PBTTT and F4TCNQ. *Macromolecules* **2014**, *47* (19), 6836−6846.